Published in Physica D (2009), vol. 238, no. 11-12, pp. 962-968
http://dx.doi.org/10.1016/j.physd.2008.08.003

The effect of tissue geometry on the activation recovery interval of atrial myocytes

A. van Oosterom*, V. Jacquemet+

* Centre Hospitalier Universitaire Vaudois (CHUV), Lausanne, Switzerland, + Signal Processing Institute, Ecole Polytechnique Fédérale de Lausanne (EPFL), Lausanne, Switzerland

***Abstract*—The propagation of electric activity inside a realistically-shaped, thick-walled model of the atria was studied. The membrane kinetics was based on the formulations of Courtemanche, Ramirez and Nattel. In spite of the assumed uniformity of all kinetics parameters, diffusion parameters, the activation recovery intervals revealed values in a range of about 20 ms, having a clearly distinct spatial distribution, with higher values close to the site of activation and lower ones at sites where activation ends. This paper presents an analysis of this phenomenon based on similar observations made on propagation along the classic models of cable and disk, as well as along the surface of a spherical shell and a diabolo-shaped shell. Propagation in the latter three geometries is treated under axial-symmetric conditions, for which dedicated analytical expressions of the diffusion term are described. The results indicate that the major effects can be directly attributed to step discontinuity in the conductivity of the medium surrounding the locations of initial and final depolarization. Overall geometry of the myocardial wall determines the smooth distribution of activation recovery intervals in the medium, showing local maxima around the points of initiation and local minima at locations where depolarization ends. The points are determined by the location of the stimulation sites involved and overall tissue geometry.**

***Index Terms*—Activation recovery interval, isotonic load, velocity of repolarization, curvature.**

[1]

I. Introduction

In the past, numerous studies have been performed on the spatial distribution of the action potential duration (APD) in the myocardium or, its electro-physiologically more relevant variant, the functionally refractory period (FRP). The latter has been shown to be highly correlated with the more directly related activation recovery interval (ARI) [1]. These studies involved a variety of animal experiments as well as computer simulations using a variety of large scale numerical models. The latter comprised differences in tissue modeling (isotropy, inhomogeneity, geometry) as well as the modeling of the ion kinetics at the membrane level. The issue addressed was the relationship between these tissue properties, as well as those of the activation sequence, on the distribution of the parameter (APD, FRP, ARI) taken to be the marker of the duration of local recovery, e.g., [2–5].

Our interest in this topic stems from our observations made on the results from simulated electrocardiographic signals associated with the normal activity of the healthy atrium [6]. In one of these simulations uniformity was assumed of all the kinetics parameters as well as of the isotropic conductivity parameters inside the atrial wall (wall thickness approx. 2 mm). In spite of the assumed uniformity, the ARI values had a range of about 20 ms, having a distinct spatial distribution, with longer values close to the site of activation and shorter ones at sites where activation ends [7]. The simulations were based the on membrane kinetics formulated by Courtemanche, Ramirez and Nattel [8], which is referred to in this paper as the CRN model. This is one of the most complete models available of the kinetics of human atrial myocytes.

The paper includes the documentation and analysis of spatial ARI distributions in the classic models of propagation along a cable and disk, as well as on a spherical shell and a diabolo-shaped shell. These configurations were selected in order to examine in how far curvature of the wave front or of tissue geometry might be involved in the observed distribution of the ARI. Propagation in the latter three geometries is treated for axial-symmetric stimuli, for which dedicated analytical expressions for handling the diffusion term are described. This permitted us to solve the essentially 2-D problems by means of their 1-D equivalents. The simulations were carried out in homogeneous, isotropic media, thus excluding the possibility of a confounding effect of either inhomogeneities and/of anisotropy.

Throughout the paper, the term propagation is used in reference to the depolarization process and, v denotes the velocity of propagation of its wave front.

[1]Corresponding address: EPFL-STI-IEL-LTS1; ELD241 (Bâtiment ELD) Station 11; CH1015. Lausanne, Switzerland. Tel.+41 21 6932708
E-mail addresses: adriaan.vanoosterom@epfl.ch, vincent.jacquemet@a3.epfl.ch

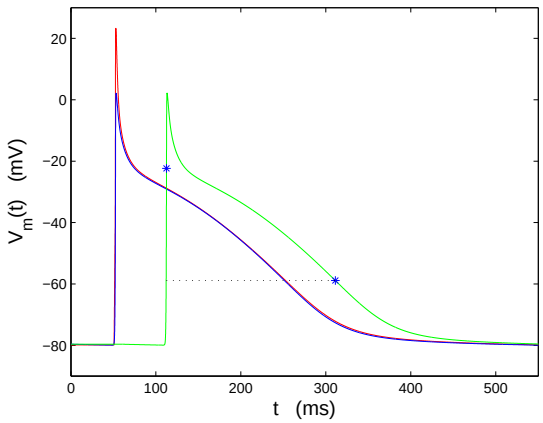

Fig. 1. TMP wave forms based on the CRN kinetics. Left traces: TMP at the stimulus site (peaked version) with superimposed, after lining up its timing, the TMP at some distance from the stimulus site propagating alone a linear cable at a locally uniform velocity of 0.75 m/s. Right trace: the propagated TMP at its proper timing; asterisks denote the inflection points, the dotted line the corresponding ARI value (approx. 200 ms).

II. Methods

A. Propagation

The propagation of the electric activity following a stimulus was computed by means of the standard reaction diffusion expression, the partial differential equation

$$C_{\rm m}\frac{\partial V_{\rm m}(\vec{r},t)}{\partial t} = S_{\rm v}^{-1}\ \nabla\cdot\sigma(\vec{r})\,\nabla V_{\rm m}(\vec{r},t)+I_{\rm stim}(\vec{r},t)-I_{\rm ion}(\vec{r},t), \quad (1)$$

where $V_{\rm m}(\vec{r},t)$ denotes the transmembrane potential at location $\vec{r}$ at time t, $C_{\rm m}$ the membrane capacitance (unit: F m^{-2}), $S_{\rm v}$ the cell's membrane-surface-to-volume ratio (unit: m^{-1}), $\sigma(\vec{r})$ the electric conductivity of intracellular the medium (unit: S m^{-1}), and $I_{\rm stim}(\vec{r},t)$ the stimulus current density injected into the intracellular medium. The function $I_{\rm ion}(\vec{r},t)$ (unit: A m^{-2}) is the current density generated by the active processes (ion-kinetics) at membrane location $\vec{r}$. In a cylindrically shaped fiber with radius a, $S_{\rm v}$ is proportional to $1/a$.

Formulation (1) represents the mono-domain approximation of the bi-domain formulation governing the propagation of the cardiac impulse in the myocardium, with $\sigma(\vec{r})$ assumed to be isotropic [9]. By convention, the voltage difference $V_{\rm m}(\vec{r},t)$ is taken to be positive if the interior of the cardiac myocyte is positive with respect to its exterior;

The term $S_{\rm v}^{-1}\ \nabla\cdot\sigma(\vec{r})\,\nabla V_{\rm m}(\vec{r},t)$ in Eq. 1 expresses the flow of current $I_{\rm m}(\vec{r},t)$ (unit: A m^{-2}) toward any membrane patch in the intracellular domain resulting from the interaction with the transmembrane potential at neighboring patches, generally referred to as representing isotonic interaction, or as the diffusion term. In the absence of external stimuli, $I_{\rm m}(\vec{r},t)$ is also the outward current density entering the extracellular domain (conservation of charge). By applying the divergence operator we have at any moment t

$$\begin{aligned} I_{\rm m}(\vec{r}) &= S_{\rm v}^{-1}\ \nabla\cdot\sigma(\vec{r})\,\nabla V_{\rm m}(\vec{r}) \\ &= S_{\rm v}^{-1}\left(\nabla\sigma(\vec{r})\cdot\nabla V_{\rm m}(\vec{r})+\sigma(\vec{r})\nabla^2 V_{\rm m}(\vec{r})\right). \quad (2)\end{aligned}$$

If σ is uniform, $\nabla\sigma(\vec{r})=0$, leaving just the term involving the Laplacian.

In a homogeneous medium Eq. 2 generally applies. Propagation may be set up in the medium by the application of a stimulus $I_{\rm stim}(\vec{r},t)$. The propagation may be sustained, depending on the stimulus strength and the nature of the membrane's ion kinetics. As is well known (see, e.g. [10]), if sustained, the uniform propagation velocity involved needs to satisfy

$$v^2 \propto D = \frac{\sigma}{C_{\rm m}S_{\rm v}}, \quad (3)$$

in which D denotes the effective diffusion coefficient [11].

When using realistic values $\sigma = 4\ 10^{-4}$ S/mm, $S_{\rm v}^{-1} = 5\ 10^{3}$ mm and $C_{\rm m} = 10^{-8}$ F/mm^2, one finds $D = 0.2$ mm^2/ms, for which the CRN kinetics generated a propagation velocity in the order of $v = 1$ m/s. Other values of v were implemented by scaling D. For $S_{\rm v}^{-1}$ and $C_{\rm m}$ remaining constant, this implied a scaling of the σ only, reflecting, e.g., differences in intercellular coupling.

B. Boundary effects

In a bounded tissue, as is the myocardium, the conductivity of the intercellular space is obviously bounded. The intracellular medium may then be considered as an infinite space in which the conductivity of its region beyond the boundary is zero (the so-called sealed-end condition) and the intracellular domain can no longer be considered as homogeneous. For some stimulus/tissue configurations the identification of the location of the discontinuity in conductivity is evident, e.g. at both ends of a finite linear cable. Wave front collisions may be treated by introducing similar, virtual discontinuities. In regard to the cable this has been described previously (e.g., [12, 13]). The finite cable is included in the treatment presented below in order to serve as the reference for the interpretation of the results related to the more complex configurations. For three of these, dedicated analytical expressions for the diffusion term are described for axial symmetric source/model configurations, which use specific variants of the surface gradient operator $\nabla_{\rm S}$ and the surface Laplacian operator $\nabla_{\rm S}^2$, expressed in locally orthogonal surface coordinates [14].

1) finite linear cable: We consider a cable segment of length L placed along the x-axis, with its end points at $x = 0$ and $x = L$. The step-like discontinuities in the conductivity at these points give rise to contributions of the gradient term in Eq. 2 equal to $\delta(x,0)\sigma\vec{1}_x \cdot \nabla V_{\rm m}(x)$ and $-\delta(x,L)\sigma\vec{1}_x \cdot \nabla V_{\rm m}(x)$, respectively. The notation $\vec{1}_x$ expresses a dimensionless unit variable directed along the variate x. Below, a similar notation is used for some other variates. The delta functions force conditions $\nabla V_{\rm m}(x) = 0$ at both $x = 0$ and $x = L$.

2) disk: Next, we consider a (flat) disk with radius R. Most papers dealing with this configuration have expressed the basic elements of the diffusion term, the gradient and the Laplacian of this 2-D problem, in Cartesian coordinates. A more appropriate coordinate system is the one using the axial coordinates r and ϕ, defined by $r = \sqrt{x^2+y^2}$ and $\phi = \arctan(y/x)$. These facilitate the treatment of the major boundary condition at $r = R$ (zero normal gradient, implementing the assumption of zero current flow between the passive intracellular domain and the extracellular domain at the tissue boundary. In these coordinates the surface gradient reads:

$$\nabla_{\rm S} = \vec{1}_r \frac{\partial}{\partial r} + \vec{1}_\phi \frac{1}{r}\frac{\partial}{\partial \phi} \tag{4}$$

and the surface Laplacian:

$$\nabla^2_{\rm S} = \frac{1}{r}\frac{\partial}{\partial r} + \frac{\partial^2}{\partial r^2} + \frac{1}{r^2}\frac{\partial^2}{\partial^2 \phi}. \tag{5}$$

If the stimulus involved has axial symmetry as well, as holds true for the cases reported on in this paper, the final terms in (4) and (5) vanish. The full expression for the diffusion term reads

$$I_{\rm m}(r,t) = S_{\rm v}^{-1}\sigma\left(\frac{1}{r}\frac{\partial}{\partial r}V_{\rm m}(r,t) + \frac{\partial^2}{\partial r^2}V_{\rm m}(r,t)\right). \tag{6}$$

Note the appearance of the first derivative in this expression, in spite of the homogeneous conductivity.

The boundary conditions of a zero gradient of $V_{\rm m}$ now have to be satisfied at $r = 0$, the center of the disk, and $r = R$, its rim.

3) spherical shell: For a spherical shell with radius R, having homogeneous (surface) conductivity, we base the surface coordinates on the spherical coordinates ϕ and θ.

For axial symmetric stimulus configurations this yields

$$I_{\rm m}(s,t) = S_{\rm v}^{-1}\sigma\left(\frac{1}{R}\cot(s/R)\frac{\partial}{\partial s}V_{\rm m}(s,t) + \frac{\partial^2}{\partial s^2}V_{\rm m}(s,t)\right), \tag{7}$$

with $s = R\,\theta$.

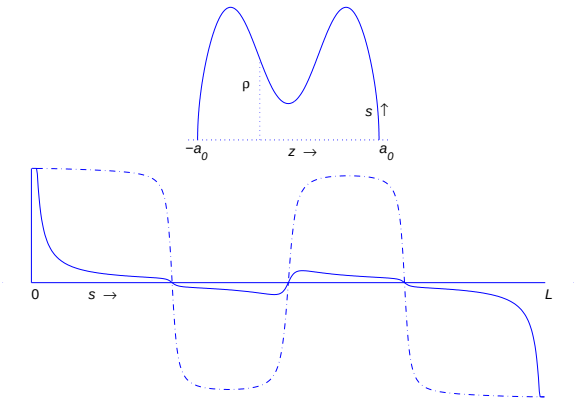

Fig. 2. Diabolo. Upper contour: the function $\rho(z)$ specifying the diabolo as a surface revolution about the z-axis. Below: dash-dot trace: the function $\frac{\partial \rho(s)}{\partial s}$ as in Eq. 9 along its trajectory s, the straightened contour of the diabolo. The solid line depicts the same function scaled by $1/\rho(s)$, truncated at the level of the unit vertical scale indicated on the left;

4) diabolo-shaped shell: A diabolo-shaped shell was defined, with its contour expressed in the cylindrical coordinates ρ, z and ϕ ($\rho = \sqrt{x^2+y^2}$, $\phi = \arctan(y/x)$). The length of the radius vector $\vec{r}$ was specified by

$$r(z) = a_0 + a_3\cos(3/2\,\pi\, z/a_0). \tag{8}$$

This type of geometry permits the study of the relationship of wall curvature on the variable of interest (ARI). Its shape has axial symmetry; for $a_3 = 0$ it reduces to a sphere with radius a_0.

The axial symmetry of the diabolo permits the use of the same surface coordinates as used for the sphere: s and ϕ, with s the distance over the surface between its "North Pole" (at $z = a_0$ and $\rho = 0$) and any point $\vec{r}$ while traveling along a "meridian".

Since the stimulus configuration too has axial symmetry, the diffusion term reads

$$I_{\rm m}(s,t) = S_{\rm v}^{-1}\sigma\left(\frac{1}{\rho(s)}\frac{\partial \rho(s)}{\partial s}\frac{\partial}{\partial s}V_{\rm m}(s,t) + \frac{\partial^2}{\partial s^2}V_{\rm m}(s,t)\right). \tag{9}$$

By interpreting ρ as proportional to the length of a propagating wave front, and s as the variate along which it travels, Eq. 9 comprises all three other expressions for the diffusion term discussed above. To show this for the cable we use $\rho = $ constant and $s = x$, for the disk (6) we take $\rho = 2\pi r$ and $s = r$, and for the sphere (7) we take $\rho = 2\pi R\sin(s/R)$ and $s = s$.

C. Ion kinetics

The CRN ion kinetics model takes into account the instantaneous conductance of 12 different types of ionic channels, the variations in Ca^{2+}, Na^{+} and K^{+} intracellular concentrations, and the calcium dynamics in the sarcoplasmic reticulum.

The parameter setting used in our work complied for the greater part with the specifications in the original publication [8]. The application to the problem in hand relied on the availability of fully stationary solutions. The existence of stable solutions for the CRN kinetics model has recently been demonstrated [15]. The stable solutions employed were realized by determining, for each of the individual pacing intervals studied, the corresponding initial conditions of all state variables. These were tuned to the value used for the calcium conductance $g_{\mathrm{CaL}} = 0.0619$ nS/pF, which is 50 % of the value specified in the CRN paper. In this way the resulting wave forms (Fig. 1) of the simulated transmembrane potentials (TMPs) resemble more closely the literature data related to atrial myocytes [16].

D. Numerical methods

The numerical handling of the diffusion part of the reaction diffusion equations was based on the Crank-Nicholson method [17], with a uniform space step of 0.15 mm. Most of the results presented below involved $N = 601$ nodes. The stimulus was applied to the first node, all activations terminated at node 601. Note that for the disk, because of the 1-D handling of the problem, a single node represented its edge. The time step used in the forward Euler procedure was 10 μs.

The diffusion term (Eq. 9) was represented by the sum of two tri-diagonal matrices of size $N \times N$: $\mathbf{D} = \mathbf{D1} + \mathbf{D2}$. Matrix $\mathbf{D2}$, approximating the second order spatial derivatives, was set up in the usual manner: it had elements -2 at its main diagonal and elements 1 at the sub-diagonals (first order numerical approximation to the second derivative). Matrix $\mathbf{D1}$, represented the gradient term (excluded for the cable). The main diagonal of $\mathbf{D1}$ was taken to be zero, the upper sub-diagonal contained values 0.5 only; for the lower these value were -0.5 (second order approximation to the first derivative). Both matrices were scaled as specified in Eqs. 6, 7 and 9, respectively. Matrix $\mathbf{D}$, scaled by a factor setting the desired velocity (Eq. 3). The boundary condition was handled by replacing the first two elements of row 1 and the final two elements of row N by appropriately scaled variants of [-1 1] and [1 -1], respectively. This also overruled the singularities at these end points cropping up in $\mathbf{D1}$.

The code (implemented in Matlab) was validated by comparing its output with that produced by using a dense triangulation of the respective surfaces, implemented in C^{++}.

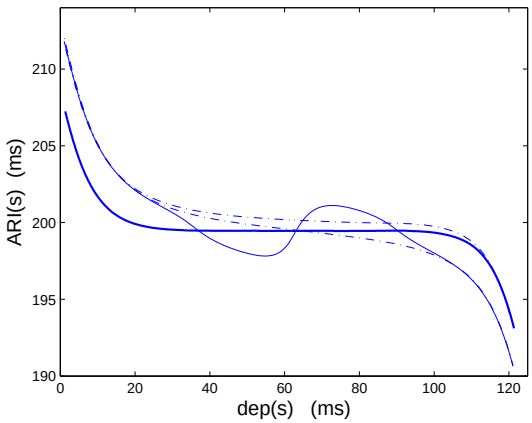

Fig. 3. $ARI(s)$ plotted as a function of $dep(s)$ for the cable (heavy solid line), the disk (upper dash-dot line), the sphere (lower dash-dot line)) and the diabolo profile (thin solid line).

E. Data analysis

1) Determining the ARI: At any node of the discretized geometries, the marker for the local activation time was taken to be that of the inflection point of the TMP, denoted as $dep(s)$. Similarly, the marker for the timing of repolarization used, $rep(s)$, was the inflection point of the final part of the downslope of the TMP. The interval between these markers is the activation recovery interval: $ARI(s) = rep(s) - dep(s)$ (Fig. 1). This interval has been shown to be closely correlated to the refractory interval, the interval of direct interest in any propagation study [1, 18]. The timing of $rep(s)$ corresponds to the timing of the maximum of $|I_C| = C_{\mathrm{m}}|\frac{\partial V_{\mathrm{m}}(t)}{\partial t}|$, and corresponds generally to the maximum magnitude of the total ion current during repolarization, as well as to the starting point of the upslope of the gating variables h and j that open the gates of the channel conductance for the sodium current I_{Na} in the CRN kinetics.

2) Geometry scaling: The respective geometries were scaled such that the length of the trajectory attained a desired value L. The trajectory of the diabolo specified in Sect. II-B4, Eq. 9, with a_0=15.8867 mm and $a_3 = 0.6a_0$, resulted in a path length of $L = 90$ mm. The shape of this contour is depicted on the upper panel of Fig. 2. For the disk we have simply: $L = R$, the radius of the disk, and for the spherical shell: $L = \pi R$, with R its radius.

3) Parameter settings: The simulations were carried out for a wide range of the parameters involved. Unless specified otherwise, the results presented in Sect. III relate to periodic pacing at intervals P= 500 ms by square current impulses of 2 ms duration (1 ms for the cable), having strengths of 1.2 times

the respective stimulus thresholds; moreover $L = 90$ mm and $v = 0.75$ m/s.

III. Results

The basic TMP wave form of a paced, single unit (cell) based on the CRN formulation with the reduced g_{CaL} value is shown in Fig. 1. The solutions were stable for values of the pacing interval P over a range of [273-3000] ms. The function $ARI(P)$ could be described accurately by

$$ARI(P) = 222.4 - 51\exp((275 - P)/303) \qquad (10)$$

ms; the maximum absolute value of the observed difference was 0.78 ms.

The wave form of a TMP propagating along an infinite uniform cable at a location far from the stimulus site is also shown in Fig. 1. This solution is referred to as $\overline{V}_{\mathrm{m}}(s,t)$. The figure includes its version lined up with the timing of the (stimulated) single unit. During the major part of repolarization, the wave forms of single unit and propagating TMPs were almost identical; the ARI value (199.45 ms) of the propagating TMP was about 0.4 ms smaller than that of the single unit.

In single cells, $I_C = C_{\mathrm{m}}\frac{\partial V_{\mathrm{m}}(t)}{\partial t} = -I_{ion}(t)$ (Eq. 1), since the diffusion term is absent. The observed similarity indicates that during uniform propagation, the polarizing part of $I_{\mathrm{C}} = I_{\mathrm{m}} - I_{\mathrm{ion}}$ must have been nearly the same as in the single unit. The monitoring of these individual currents revealed that throughout repolarization, the magnitude of $I_{\mathrm{m}}(s)$ was about 10% of that of I_{ion}. In the bounded geometries, throughout repolarization, $I_{\mathrm{m}}(t)$ was positive near the stimulus site and negative near the end point; mid-cable it was biphasic (negative first), having amplitudes that were about 20 $\%$ of the endpoint values.

Following a periodic stimulation at a single site, the reported data for all four cases studied are: $dep(s)$, $rep(s)$ and $ARI(s) = rep(s) - dep(s)$. In all of the simulations, the velocity of the propagation of the excitation along all geometry variants was found to be uniform at the space and velocity scales studied. Minor deviations were observed at a sub-mm scale near both end points of s. Note that for the sphere and the diabolo these relate to the virtual end points at their "South Pole", for the disk it relates to its rim. These deviations were discarded in the subsequent analysis, and hence, for all values of the parameters L and v, we will take $dep(s)$ as increasing linearly with s.

The $ARI(dep(s))$ functions observed for L=90 mm are shown in Fig. 3. Because of the uniform value of v the abscissa, $dep(s)$, used in this figure is directly proportional to s. The respective ARI values at the stimulus site, mid point and end point of the trajectory are listed in Table. I.

case	$ARI(0)$	$ARI(45)$	$ARI(90)$	range
cable	207.25	199.46	193.11	14.14
disk	211.71	200.17	193.27	18.44
sphere	212.01	199.49	190.68	21.33
diabolo	211.80	199.28	190.64	21.17

TABLE I
FOR EACH OF THE FOUR FUNCTIONS DEPICTED IN FIG. 3 THE VALUES OF ARI IN MS AT $s = 0$, (STIMULUS SITE), $s = L/2$ (HALF WAY), $s = L$ (TERMINATION OF THE DEPOLARIZATION) AND THE RANGE; L=90 MM, v=0.75 M/S.

The $ARI(s)$ function observed for the finite cable was fitted by the sum of two exponential functions, shifted to the $ARI(45)$ level. The initial and final time constants τ_1 and τ_2, found were 6.9 and 6.1 ms, respectively. At the propagation velocity v=0.75 m/s specified, these values correspond to space constants of 5.18 and 4.58 mm, respectively.

IV. Analysis

A. End effects on repolarization

Throughout repolarization, the ion kinetics of a membrane patch passes through an active phase, during which I_{ion} is positive. The character of the patch can be likened to a current source since the magnitude of the current generated is relatively independent of V_m.

During the repolarization phase in a fiber or a conglomerate of coupled cells, for any membrane patch P at any location, neighboring membrane patches that repolarize (slightly) later will have a higher TMP. Consequently, these will pass a (positive) current toward patch P, yielding a positive contribution to the local value of I_m at P. Since $I_C = I_m - I_{ion}$, the local repolarizing effect of I_{ion} is reduced. As long as the contribution to I_m is positive, the local repolarization process will be retarded relative to that in the infinite uniform cable, thus yielding higher values of $rep(s)$ and, hence, yielding longer values of $ARI(s) = rep(s) - dep(s)$. If patch P is one of the last ones depolarized, most neighboring patches may have attained a lower TMP and, hence, I_m will be negative. Here the local repolarization process will be accelerated, thus yielding lower values of $rep(s)$ and, hence, shorter values of $ARI(s) = rep(s) - dep(s)$.

Below, this qualitative description is backed up by a quantitative one, based on the appropriate expressions for I_m, such as Eqs. 2, 6, 7 and 9. This requires the function $V_{\mathrm{m}}(s,t)$ to be known.

For an infinite cable, with activation propagating at uniform velocity v in the positive direction along the x-axis, we have

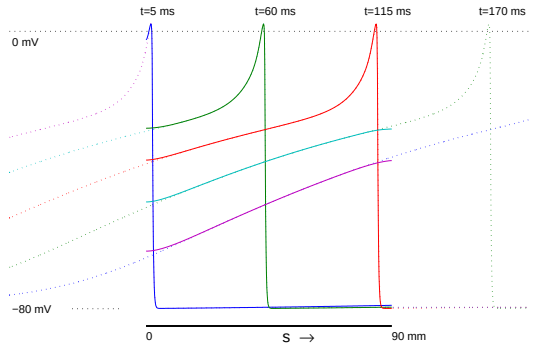

Fig. 4. Potential profiles along a linear cable at selected time intervals. Dashed lines: passage along infinitely long cable. Solid lines: stimulus applied at $t = 0$ at $s = 0$ of a finite cable; length 90 mm; propagation velocity 0.75 m/s. Note the zero gradient of the profiles near both ends of the finite cable.

$\overline{V}_{\rm m}(x,t) = \overline{V}_{\rm m}(x - vt)$. Hence the instantaneous potential profiles, propagating along the s axis, are identical to the wave form shown in Fig. 1, but for a reversed direction of the abscissa as well as its nature (distance versus time). Such profiles, at selected time instants, are depicted by the dashed lines in Fig. 4.

The corresponding values of $I_m(x)$ at any moment in time are proportional to the second spatial derivatives of these profiles (Eq. 2). Wherever these profiles curve upward for increasing s values, the second derivative is positive (hence also I_m), else it is zero (straight part of the profile) or negative.

As discussed in Sect. II-B1, the boundaries of a finite cable demand the inclusion of the constraint $\nabla V_{\rm m}|_{x=0} = 0$. The involved reaction diffusion equation was solved while including the constraint. The results are included in Fig. 4 (solid lines). As can be seen, the effect on the profiles is small, the most prominent differences showing up at the two end points, where the local gradients of the bounded solutions are indeed zero. Note that the effect of the boundary at s=0 increases the local upward curvature of the profile and that at $s = L$ the downward curvature of the profile is increased, both relative to the infinite cable profiles.

Based on this observation, as well as on the observed exponential nature of the decay in the $ARI(dep)$ functions, the following analysis can be justified. It is included here in an attempt to evaluate the influence of v and L.

We consider the application of a stimulus at location $x = 0$, being the end of a semi-infinite cable extending along the positive x-axis. The solution to Eq. 1 for this configuration is written as

$$V_{\rm m}(x,t) = \overline{V}_{\rm m}(x,t) + \Phi(x,t). \tag{11}$$

The first term on the right-hand side denotes the solution to Eq. 1 for an activity propagating uniformly along an infinite cable, initiated at $x = -\infty$ and $t = -\infty$. We denote the corresponding membrane current as $\overline{I}_{\rm m}(x,t)$.

The function $\Phi(x,t)$ denotes a perturbation, taken to express the effect of the boundary conditions. The latter may be expected to be small (Fig. 4). Following the passage of the wave front $I_{\rm stim} = 0$ and substitution of Eq. 11 into Eq. 1 demands that $\Phi(x,t)$ should satisfy

$$C_{\rm m}\frac{\partial\Phi(x,t)}{\partial t} = S_{\rm v}^{-1}\,\sigma\,\frac{\partial^2\Phi(x,t)}{\partial x^2}. \tag{12}$$

The small values of the differences between $V_{\rm m}(x,t)$ and $\overline{V}_{\rm m}(x,t)$ as observed in Fig. 4, as well as their spatial profiles, indicate that the solution to Eq. 12 may be approximated by the one based on the method of separation of variables, which leads to an approximate solution of the type

$$\Phi(x,t) = \Phi_0(t)\exp(-x/\lambda), \tag{13}$$

with $\lambda \propto \sqrt{\sigma}$, as is shown in Sect. 7.3.2 of [10].

Since, for $t > 0$, the boundary condition at $x = 0$ demands that $\nabla V_{\rm m}(x,t)$ is zero, we must have, at $x = 0$, $\nabla\Phi(x,t) = -\nabla\overline{V}_{\rm m}(x,t)$. This leads to the identification of $\Phi_0(t)$, on the basis of which we find

$$\Phi(x,t) = \lambda\nabla\overline{V}_{\rm m}(x - vt)|_{x=0}\exp(-x/\lambda), \tag{14}$$

By substitution this solution in Eq. 12 we see that for $t > 0$ and $x > 0$ the right-hand side may be identified as a virtual current source (a surface density)

$$I_{\rm vir}(x,t) = \frac{\sigma}{S_{\rm v}\lambda}\nabla\overline{V}_{\rm m}(x - vt)|_{x=0}\exp(-x/\lambda), \tag{15}$$

whose strength is added to $\overline{I}_{\rm m}(x,t)$.

As a final step the total charge (surface density) $Q(x)$ generated by $I_{\rm vir}(x,t)$ at any location x during repolarizarion is found by integration of $I_{\rm vir}(x,t)$ over time. Based on the uniform propagation of $\overline{V}_{\rm m}(x,t)$ we may exchange the spatial gradient by the temporal derivative ($\frac{\partial}{\partial x}\overline{V}_{\rm m}(x,t) = -\frac{1}{v}\frac{\partial}{\partial t}\overline{V}_{\rm m}(x,t)$) and so we find

$$Q(x) = \frac{\sigma}{vS_{\rm v}\lambda}V_{\rm D}\exp(-x/\lambda), \tag{16}$$

with $V_{\rm D}$ denoting the absolute value of the total excursion of the downslope of the TMP, say, $|-80|$ mV (Fig. 1).

The same type of exponential decay can be expected at the end point of a finite cable segment, but for an opposite sign and a decay in the reverse direction. Positive values of $Q(x)$ cause a local retardation of the repolarization process relative *to that in the infinite cable*, negative values its acceleration. Although the local effects may be small, their cumulation along the cable may cause a substantial difference in the ARI values, as is illustrated by the heavy solid line in Fig. 3.

B. Effects of shape

The $ARI(dep)$ results documented in Fig. 3 exhibit distinct differences with those observed for the cable. Recall that the trajectories involved were of equal length and that the velocities along the paths were tuned to be equal. All deviations from the results found for the cable can be explained on the basis of additional contributions stemming from the gradient of the local TMP as expressed in Eqs. 6, 7 and 9. The effect can be explained in a way similar to the one described for the cable.

As an example we consider the case of the disk, Eq. 6. Here the total contribution during repolarization at site r is a locally weighted gradient of the local TMP. After exchanging spatial and temporal differentiation (uniform propagation), integration over time of the additional current yields

$$Q(r) = \frac{\sigma}{vS_{\mathrm{v}}r}V_{\mathrm{D}}. \tag{17}$$

An inspection of the upper dash-dot line in Fig. 3 exhibits indeed an additional delay of the repolarization moment, and correspondingly, an additional increase of the ARI values at the stimulus site (of 4.5 ms), which decays as $1/r$.

The same explanation can be given for the results observed on the sphere (lower dash-dot line in Fig. 3). Here the spatial weighting function is $\frac{1}{R}\cot(s/R)$, yielding an additional increase of the $ARI(s)$ values at the stimulus site of 4.75 ms, and a similar reduction at the terminal point of the activation. Halfway, at $s = R\pi/2$, the weighting function is zero; the local slope of the curve is proportional to the gradient of $\cot(s/R)/R$, viz, proportional to $-1/R^2$.

For the diabolo shape, no simple analytical expression could be found for the weighting function in Eq. 9 on the basis of the definition of its contour (Eq. 8). Instead, a numerical procedure was used, the result of which is depicted in the lower panel of Fig. 2. The solid line represents the weighting function $\frac{1}{\rho(s)}\frac{\partial\rho(s)}{\partial s}$, the dashed line, the variant leaving out the scaling factor $1/\rho(s)$. The effect of the weighting function is clearly expressed in the thin solid line shown in Fig. 3. Once again, the additional effect of the weighted version of V_{D} is greatest at $s = 0$ and $s = L$. The positions of the zero crossings of the traces shown in the lower panel of Fig. 3 coincide with those of the peaks and valleys of the contour shown in the upper panel of Fig. 2. The $ARI(dep)$ values at these locations coincide with those of the cable. This clarifies the intriguing nature of the function $ARI(dep)$ for this case.

The singularities involved in the weighting functions are of the same type: $1/r$. Their impact is neutralized by the zero gradient boundary condition.

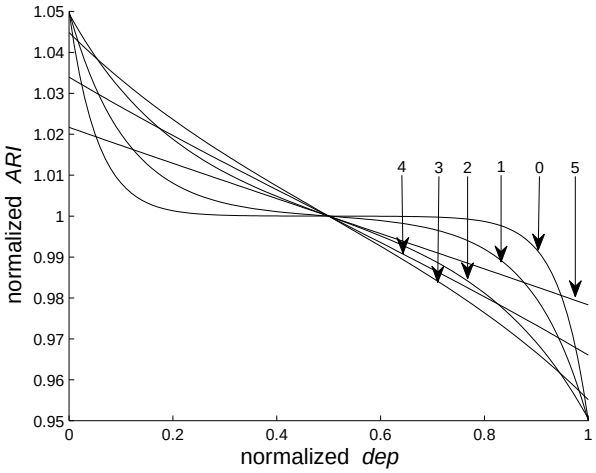

Fig. 5. Normalized $ARI(dep)$ curves of the finite cable, based on the the difference of two exponentials (Eq. 24). The labels of the traces (k) also denote powers of two specifying $\mu = 2^k/18.2$; $\Delta_\alpha = 0.05$

C. Effects of velocity and size

Several simulations were run, each involving different settings of the parameters L and v, while keeping all others constant. Below we use s as the distance along the trajectories.

1) Velocity: In all simulations, at all values of the propagation velocity v tested, the ARI values half-way along the trajectory were identical. In the following analysis we use the fact that, since $\lambda^2 \propto \sigma$ (passive diffusion) and $v^2 \propto \sigma$ (Eq. 3), we must have

$$\lambda = \tau v, \tag{18}$$

with τ a proportionality constant. Moreover, we take the shape of $Q(s)$ as discussed in the previous sections as describing $\Delta ARI(dep) = ARI(dep) - ARI_{\mathrm{i}}$, with ARI_{i} denoting the ARI value in the infinite uniform cable.

Applied to the semi-infinite cable, Eq. 16, we have

$$\Delta ARI(dep) \propto \frac{\sigma}{v\lambda}\exp(-s/\lambda), \tag{19}$$

and by inserting the proportionalities listed above,

$$\Delta ARI(dep) \propto \exp(-dep/\tau), \tag{20}$$

which indicates that $\Delta ARI(0)$ is independent of velocity, as is the time constant of the exponential decay (Eq. 18). On the basis of Eq. 20, the τ, introduced as just a proportionality constant, may now be likened to the parameters τ_1 and τ_2 introduced in Sec. III for describing the experimental results for the cable (Fig. 4).

In a similar application, now to the sphere (Eq. 7), we find after inserting the proportionalities,

$$\Delta ARI(dep) \propto \frac{\sigma}{vR} \cot(\frac{v\ dep}{R}). \quad (21)$$

It may seem as if here $\Delta ARI(0)$ might depend on v. However, all simulation results showed essentially identical values. The explanation is found by using the series expansion of $\cot(\frac{v\ dep}{R})$ for small values of dep. Inserting just the first term, we see that

$$\Delta ARI(dep) \propto \frac{\sigma}{v\ R} \frac{R}{v\ dep} = \frac{\sigma}{v^2\ dep}, \quad (22)$$

which is independent of v, since $v^2 \propto \sigma$ (Eq. 3). As before, the remaining singularity, $1/dep$, is absorbed by the zero gradient of the local transmembrane potential of the "real world" solution.

2) Size: For each of the three geometries studied, and for all values of v and L, taken here as a measure of the total length of the depolarization trajectory, it was observed that the shapes of their respective $ARI(dep)$ curves could be expressed by a single parameter. Below, this is explained and illustrated on the basis of the results pertaining to the cable.

Let x denote the normalized variable $x = dep/dep_L$ ($dep_L = L/v$). By inserting x into Eq. 20 we have

$$\Delta ARI(x) \propto \exp(-\frac{x}{\tau\ dep_L}). \quad (23)$$

Since τ as introduced in Eq. 20 is a constant, we see that the shape of $\Delta ARI(x)$ depends on a single parameter, which we define as $\mu = \tau L/v$: all shapes of $\Delta ARI(x)$ are proportional to the ratio $L/v = dep_L$ only.

Below, we apply this result to both ends of the cable and introduce $\alpha(x) = ARI(dep)/ARI(dep(L/2))$. Based on the preceding analysis we express the $ARI(dep)$ data by a family of the curves (Fig. 5) specified by

$$\alpha(x) = 1 + \Delta_\alpha(\exp(-x/\mu) - \exp((x-1)/\mu)), \quad (24)$$

with $\Delta_\alpha = \alpha(0) - 1$, and μ the parameter defining their shape. The individual traces shown relate to multiples of 6.6/120, based on the value of 6.6 identified in the result of the fitting procedure applied to the cable data shown in Fig. 3. By decreasing dep_L the shape parameter μ increases. Initially, the two exponentials shown in Fig. 3 can be recognized separately; for higher values of μ the initial, the linear part of the exponentials are expressed more and more clearly and their combinations tend to become linear. Significantly, for these smaller values of dep_L, as is to be expected if L (overall heart size) is reduced [19], the total range of the ARI values tends to zero, with all ARI values equal to that of the single unit value ($L = 0$).

V. Discussion

The simulations of propagated activity and its subsequent recovery provided a qualitative explanation for the observed spatial distribution of ARI values. All simulations performed in this study were also carried out while using an entirely different kinetics mode: the original, classic model of Beeler and Reuter [20]. Quantitative differences were found: for the cable (BR): higher mid-cable ARI values (250 ms), a smaller range $\Delta(ARI)$ (8.5 ms), and a smaller value of τ (4 ms), compared to the CRN-based results: ARI= 199 ms, $\Delta(ARI)$=14 ms and τ=4.9 ms (mean of τ_1 and τ_2 shown in the results section). However, all qualitative results were the same, permitting the same interpretation as described in Sect. IV. The method used for analyzing the end effects (Sect. IV-B) is similar to the one used by Steinhaus *et al.* [13] in their interpretation of electrophysiological data. In their numerical evaluations applied to the cable, they used the kinetics model proposed for Purkinje fibers by MacAllister *et al.*[21]for which they reported end effects of the order of 5 ms.

Along the trajectories, at the spatial scale studied, the velocity of the propagating wave front was almost uniform, unaffected by differences wave front or geometry curvature. The minor deviations observed were located at a sub-mm scale near both end points of s, as could be expected [22].

The major deviations from the observed ARI values relative to their mid-interval ARI values were invariably located at points where depolarization started and ended (Table. I). Recall that the conductivity along the trajectory of depolarization was uniform, as were the intrinsic parameters of the ion kinetics model. This was also observed in our simulations in thick-walled variants of the same 2-D geometries as well as in a realistic atrial geometry, in which multiple simultaneous stimuli were applied and, consequently, multiple end points of depolarization [7]. These observations stress the dominant effect of the depolarization sequence on the spatial distribution of the subsequent time course of local repolarization, as has been previously reported [23].

With their lower ARI values, regions around such end points of depolarization are likely to play a role in instabilities observed in atrial electric activity.

The range of the major deviations did not depend on propagation velocity, type of geometry, and overall scale of the geometry. The latter indicates that, whatever measure of curvature is used for characterizing either wave front or geometry of the tissue boundary, the influence of curvature on these deviations is secondary.

The shapes of the $ARI(dep)$ functions were specific for "tissue" geometry (Fig. 3). These were reflecting the nature of

the factor $\frac{1}{\rho(s)}\frac{\partial\rho(s)}{\partial s}$ weighting the gradient related contribution to the diffusion term (Eqn. 9). For overall size L greater than that of the diffusion based length (λ) the mid-interval ARI values were close to the value observed for the uniform infinite cable.

The gradient related term used in Eq. 9 expresses the effects of geometry. It is mathematically equivalent to those used in various early studies in which the effects of local inhomogeneities in electric conductivity or in membrane kinetics were evaluated [12, 24]. Discussions on the effects of inhomogeneous electric conductivity along a cable are usually phrased in terms of mismatch in electric loading. The analysis presented at the end of Sect. II-B4 suggests that discussions on geometric effects may also be cast in the same terminology. An alternative interpretation follows from noting that, for uniform propagation, the factor $\frac{1}{\rho(s)}\frac{\partial\rho(s)}{\partial s}$ is proportional to the velocity of relative change of the length of the wave front.

In the application to the CRN kinetics, the use of the method of separation of variables in approximating the solution to the diffusion equation Eq. 12 were justified by the high correspondence between the ARI features observed and those of the analysis presented. Our work extends previous studies by including an analysis of the contribution of geometry-related factors. Their maximum contribution is shown to be an increase of 7 ms to 12 ms.

The results and their analysis presented here aim at providing a background for the interpretation of details in the spatial distribution of ARI values observed in electrophysiological measurements. Without a background such details may easily be attributed to other factors.

ACKNOWLEDGMENT

The authors are grateful to the anonymous reviewers for their highly pertinent criticism of a previous manuscript of this paper and their encouragement and suggestions for its improvement.

REFERENCES

[1] C. K. Millar, F. A. Kralios, and R. L. Lux, "Correlation between refractory periods and activation-recovery intervals from electrograms: effects of rate and adrenergic interventions," *Circulation*, vol. 6, pp. 1372–1379, 1985.

[2] J. A. Abildskov, "Effects of activation sequence on the local recovery of ventricular excitability in the dog," *Circ Res*, vol. 38, no. 4, pp. 240–3, 1976.

[3] T. Osaka, I. Kodama, N. Tsuboi, J. Toyama, and K. Yamada, "Effects of activation sequence and anisotropic cellular geometry on the repolarization phase of action potential of dog ventricular muscles," *Circulation*, vol. 76, no. 1, pp. 226–36, 1987.

[4] M. J. Burgess, B. M. Steinhaus, K. W. Spitzer, and P. R. Ershler, "Nonuniform epicardial activation and repolarization properties of in vivo canine pulmonary conus," *Circ Res*, vol. 62, no. 2, pp. 233–46, 1988.

[5] A. W. Cates and A. E. Pollard, "A model study of intramural dispersion of action potential duration in the canine pulmonary conus," *Ann Biomed Eng*, vol. 26, no. 4, pp. 567–76, 1998.

[6] A. van Oosterom and V. Jacquemet, "Genesis of the P wave: Atrial signals as generated by the equivalent double layer source model," *Europace*, vol. 7(Suppl.)S, pp. 21–29, 2005.

[7] van Oosterom A. and V. Jacquemet, "The QRS-integral of an Electrogram as an Indicator of the Subsequent Local Activation Duration," in *Computers in Cardiology '06*, A. Murray, Ed., vol. 33. Piscataway: IEEE Computer Society Press, 2006, pp. 669–572.

[8] M. Courtemanche, R. J. Ramirez, and A. Nattel, "Ionic mechanisms underlying human atrial action potential properties: insights from a mathematical model," *Am J Physiol Heart Circ Physiol*, vol. 275, pp. H301–H321, 1998.

[9] R. M. Gulrajani, *Bioelectricity and Biomagnetism*. New York: John Wiley & Sons, 1998.

[10] R. Plonsey and R. C. Barr, *Bioelectricity: A Quantitative Approach*. New York: Springer, 2007, third edition.

[11] A. H. Keener and A. H. Panvilov, "The Effects of Geometry and Fibre Orientation on Popagation and Extracellular Potentials in Myocardium," in *Computational Biology of the Heart*, A. V. Holden and A. V. Panvilov, Eds. Chichester: John Wiley & Sons, 1997.

[12] M. S. Spach, R. C. Barr, G. S. Serwer, E. A. Johnson, and J. M. Kootsey, "Collision of excitation waves in the dog purkinje system," *Circulation Res*, vol. XXIX, pp. 499–511, 1971.

[13] B. M. Steinhaus, K. Spitzer, and S. Isomura, "Action Potential Collision in Heart Tissue-Computer simulations and tissue experiments," *IEEE Trans Biomed Eng*, vol. BME-32/10, pp. 731–742, 1985.

[14] J. van Bladel, *Electromagnetic Fields*. New York: McGraw-Hill, 1964.

[15] V. Jacquemet, "Steady-state solutions in mathematical models of atrial cell electrophysiology and their stability," *Mathematical Biosci*, vol. 2008, pp. 241–269, 2007.

[16] H. Gelband, H. L. Bush, M. R. Rosen, R. J. Myerburg, and B. F. Hoffman, "Electrophysiologic properties of isolated preparations of human atrial myocardium," *Circ Res*, vol. 30, pp. 293–300, 1972.

[17] J. Crank and P. Nicholson, "A practical method for numerical evaluation of solutions of partial differential equations of the heat-conduction type," *Proc Camp Phil Soc*, vol. 43, pp. 50–67, 1947.

[18] C. Haws and R. Lux, "Correlation Between In Vivo Transmambrane Action Potential Durations and Activation-Recovary Intervals From Electrograms," *Circulation*, vol. 81/1, pp. 281–288, 1990.

[19] K. J. Sampson and C. S. Henriquez, "Electrotonic influences on action potential duration dispersion in small hearts: a simulation study," *Am J Physiol Heart Circ Physiol*, vol. 289, pp. H350–H360, 2005.

[20] G. W. Beeler and H. Reuter, "Reconstruction of the action potential of ventricular myocardial fibres," *J. Physiol (London)*, vol. 268, pp. 177–210, 1977.

[21] R. E. McAllister, D. Noble, and R. W. Tsien, "Recontruction of the electrical activiy of cardiac Purkinje fibres," *J. physiol*, vol. 251, pp. 1–59, 1975.

[22] V. Zykov and O. L. Morozova, "Speed of spread of excitation in a two-dimensional excitable medium," *Biophysics*, vol. 24, pp. 739–744, 1979.

[23] M. J. Burgess, L. S. Green, K. Millar, R. Wyatt, and J. A. Abildskov, "The sequence of normal ventricular recovery," *American Heart Journal*, vol. 84/5, pp. 660–669, 1972.

[24] R. W. Joyner, J. Picone, R. Veenstra, and D. Rawling, "Propagation through Electrically Coupled Cells. Effects of Regional Changes in Membrane Properties," *Circulation Res*, vol. 53, pp. 526–534, 1983.